Inorganic Chemistry

Cite This: Inorg. Chem. XXXX, XXX, XXX−XXX

Article

pubs.acs.org/IC

Crystal and Magnetic Structures and Properties of $(Lu_{1-x}Mn_x)MnO_3$ Solid Solutions

Lei Zhang,[†,‡] Andreas Dönni,[§] Vladimir Y. Pomjakushin,[∥] Kazunari Yamaura,[†,‡] and Alexei A. Belik*[,†]

[†]Research Center for Functional Materials, National Institute for Materials Science (NIMS), Namiki 1-1, Tsukuba, Ibaraki 305-0044, Japan

[‡]Graduate School of Chemical Sciences and Engineering, Hokkaido University, North 10 West 8, Kita-ku, Sapporo, Hokkaido 060-0810, Japan

[§]International Center for Materials Nanoarchitectonics (WPI-MANA), National Institute for Materials Science (NIMS), Namiki 1-1, Tsukuba, Ibaraki 305-0044, Japan

[∥]Laboratory for Neutron Scattering and Imaging, Paul Scherrer Institute, 5232 Villigen PSI, Switzerland

Supporting Information

ABSTRACT: $(Lu_{1-x}Mn_x)MnO_3$ solid solutions, having the perovskite-type structure and *Pnma* space group, with $0 \leq x \leq 0.4$ were synthesized by a high-pressure, high-temperature method at 6 GPa and about 1670 K from Lu_2O_3 and Mn_2O_3. Their crystal and magnetic structures were studied by neutron powder diffraction. The degree of octahedral MnO_6 tilting decreases in $(Lu_{1-x}Mn_x)MnO_3$ with increasing x. Only the incommensurate (IC) spin structure with a propagation vector of $\mathbf{k} = (k_0, 0, 0)$ and $k_0 \approx 0.44$ remains in $(Lu_{0.9}Mn_{0.1})MnO_3$ in the whole temperature range below the Neel temperature $T_N = 36$ K, and the commensurate noncollinear E-type structure that has been reported in the literature for undoped o-$LuMnO_3$ is not observed. $(Lu_{1-x}Mn_x)MnO_3$ samples with $0.2 \leq x \leq 0.4$ have a ferrimagnetic structure with a propagation vector of $\mathbf{k} = (0, 0, 0)$ and ferromagnetic (FM) ordering of Mn^{3+} and Mn^{4+} cations at the B site, which are antiferromagnetically coupled to a noncollinear predominantly FM arrangement of Mn^{2+} at the A site. The ferrimagnetic Curie temperature, T_C, increases monotonically from 67 K for $x = 0.2$ to 118 K for $x = 0.4$. Magnetic and dielectric properties of $(Lu_{1-x}Mn_x)MnO_3$ and a composition−temperature phase diagram are also reported.

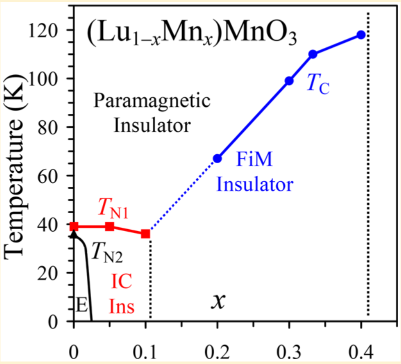

1. INTRODUCTION

Perovskite-structure rare earth (R) manganites, o-$RMnO_3$, have been a playground for solid-state and materials chemists and physicists for decades,[1−13] where "o" stands for an orthorhombic modification with space group *Pnma*. Undoped o-$RMnO_3$ manganites have only spin and orbital degrees of freedom, and they exhibit orbital order (OO) transitions at quite high temperatures (T_{OO} = 750−1500 K) and spin order transitions at much lower temperatures (with Néel temperatures T_N = 40−140 K).[7,8,11] Both T_{OO} and T_N are highly sensitive to the size of R^{3+} cations, which determines the magnitude of tilts of MnO_6 octahedra.[7,8] The tilts in turn affect the Mn−O−Mn bond angles and the strengths of nearest-neighbor (J_{13} and J_{12})[3] and next-nearest-neighbor (J_{11} and J_{14})[3] exchange interactions between Mn atoms. The ground state magnetic ordering of $RMnO_3$ also changes from A-type antiferromagnetic (AFM) ordering with spin canting for R = La−Gd, to spin spirals for R = Tb and Dy,[5,6] and to collinear and noncollinear E-type AFM ordering without spin canting for R = Ho−Lu.[10,11,13] Spiral and E-type magnetic orderings give rise to one of the largest spin-induced ferroelectric polarizations reported for type II multiferroic materials.[5,12,13]

In doped $R_{1-x}A_xMnO_3$ manganites, the charge degree of freedom appears, and a large variety of new phenomena emerges, such as colossal magnetoresistance, phase separation, a wide range of different ground states (ferromagnetic (FM) metals; charge- and orbital-ordered antiferromagnets of A-, CE-, C-, and G-types; and stripe and spin-glass states), and so on.[14−21] The concepts of double exchange, small polarons, electron−phonon, and Jahn−Teller couplings were widely developed using $R_{1-x}A_xMnO_3$ manganites as model systems.[14−16] A large number of work was devoted to the investigation of $R_{1-x}A_xMnO_3$ with large R cations, such as R = La, Pr, Nd, and Sm, and detailed composition−temperature phase diagrams were constructed.[14−18] Special regions on phase diagrams related to charge ordering were often observed near $x = 0.5$ (half doped) and $x = 1/3$ (one-third doped). On the other hand, just a few papers have been published dealing with small R cations, such as R = Tm−Lu,[19−21] and no phase diagrams have been reported.

In most of the reported cases of $R_{1-x}A_xMnO_3$, A is a nonmagnetic cation, such as A = Ca^{2+}, Sr^{2+}, and Ba^{2+}, and solid

Received: May 29, 2018

DOI: 10.1021/acs.inorgchem.8b01470

solutions usually exist over the whole concentration ranges of $0 \leq x \leq 1$ (for A = Ca and Sr).[14−18] There are some reports with A being a magnetic cation (A = Mn^{2+}).[22−25] However, by an ambient-pressure synthesis, high concentrations of Mn^{2+} at the A site of ABO_3 perovskites cannot be reached. On the other hand, we have recently found that high concentrations of Mn^{2+} at the A site can be achieved by a high-pressure synthesis method, and we prepared and investigated one-third-doped $(R_{0.667}Mn_{0.333})MnO_3$ compositions with R = Er−Lu.[26] The presence of high concentrations of magnetic Mn^{2+} cations at the A site results in different properties in comparison to doping with nonmagnetic cations for the same R cation. For example, magnetization reversal (or negative magnetization) effects and first-order spin-reorientation transitions were observed in $(R_{0.667}Mn_{0.333})MnO_3$;[26] on the other hand, no evidence for charge-ordering phenomena was detected for these one-third-doped compositions.

In this work, we report on detailed structural and magnetic properties of $(Lu_{1-x}Mn_x)MnO_3$ solid solutions with $0 \leq x \leq 0.5$, and we built a composition−temperature phase diagram. We touched an unexplored area in the field of the $R_{1-x}A_xMnO_3$ manganites.[21] First, we selected the smallest R cation (R = Lu), which is nonmagnetic, and therefore, the behavior of such systems without the influence of rare-earth magnetism can be understood. Second, we doped o-$LuMnO_3$ with a magnetic cation at the A site. The aims of this work are (1) to see the effects of A-site doping on multiferroic behavior of o-$LuMnO_3$ and (2) see the effects of A-site doping by a magnetic 3*d* transition metal on an $R_{1-x}A_xMnO_3$ phase diagram and the nature of magnetic interactions at the B site. An incommensurate (IC) spin ordering takes place in $(Lu_{0.9}Mn_{0.1})MnO_3$ in the whole temperature range below T_N = 36 K, while the IC phase locks into a commensurate noncollinear E-type structure with a large ferroelectric polarization in undoped o-$LuMnO_3$.[13] A ferrimagnetic structure is realized in $(Lu_{1-x}Mn_x)MnO_3$ with $0.2 \leq x \leq 0.4$ with a FM ordering of Mn^{3+} and Mn^{4+} cations at the B site, which are antiferromagnetically coupled with Mn^{2+} at the A site, and the ferrimagnetic Curie temperature (T_C) increases sharply with increasing *x*. All phases remain insulators below room temperature. We argued that the presence of Mn^{2+} at the A site of the samples with $0.2 \leq x \leq 0.4$ plays a crucial role in determining their magnetic structure, while the presence of Mn^{4+} at the B site of $(Lu_{0.9}Mn_{0.1})MnO_3$ keeps the IC structure. The remaining part of the paper is organized as follows. We first present details of the sample synthesis and experimental techniques in section 2. Details of nuclear (paramagnetic) structure and composition refinements and results are given in section 3.1, followed by the magnetic structure analysis in section 3.2. In section 3.3, we report and discuss magnetic and dielectric properties in connection with the magnetic structures determined. Finally, a composition−temperature phase diagram is constructed and discussed in section 3.4, and conclusions are drawn in section 4.

2. EXPERIMENTAL SECTION

$(Lu_{1-x}Mn_x)MnO_3$ samples with *x* = 0, 0.05, 0.1, 0.2, 0.3, 0.4, and 0.5 were prepared from stoichiometric mixtures of Mn_2O_3 and Lu_2O_3 (99.9%). Single-phase Mn_2O_3 was prepared from commercial MnO_2 (99.99%) by heating in air at 923 K for 24 h. The mixtures were placed in Pt capsules and treated at 6 GPa and about 1670 K for 2 h (heating time to the synthesis temperature was 10 min) in a belt-type high-pressure apparatus. After the heat treatments, the samples were quenched to room temperature (RT), and the pressure was slowly released. All the samples obtained were black pellets (quite friable in some cases).

$(Lu_{0.9}Mn_{0.1})MnO_3$ (about 4.2 g) and $(Lu_{0.6}Mn_{0.4})MnO_3$ (about 3.0 g) samples for neutron diffraction were synthesized from stoichiometric mixtures of Mn_2O_3 and hex-$LuMnO_3$ using the same synthesis conditions, where "hex" stands for a hexagonal modification (space group $P6_3cm$) of $LuMnO_3$. The use of hex-$LuMnO_3$ allows increasing the sample volume synthesized in one high-pressure, high-temperature run. About eight batches of each sample were mixed for neutron diffraction. Single-phase hex-$LuMnO_3$ was synthesized from a stoichiometric mixture of Mn_2O_3 and Lu_2O_3 by annealing in air at ambient pressure at 1423 K for 80 h with several intermediate grindings.

X-ray powder diffraction (XRPD) data were collected at RT on a RIGAKU MiniFlex600 diffractometer using Cu Kα radiation (2θ range of 8−140°, a step width of 0.02°, and scan speed of 1°/min).

Neutron powder diffraction experiments were conducted at the Swiss Spallation Neutron Source (SINQ) at the Paul Scherrer Institute (PSI). The $(Lu_{0.9}Mn_{0.1})MnO_3$ and $(Lu_{0.6}Mn_{0.4})MnO_3$ samples were measured at temperatures between 2 and 230 K using the high resolution powder diffractometer HRPT[27] and an incident neutron wavelength of about 1.89 Å (2θ range of 3.55−164.50°, and a step width of 0.05°). The diffraction patterns were analyzed by the Rietveld method using the *FullProf Suite*.[28] Possible models for the magnetic structures were deducted based on a group theory analysis using the program *BasIreps*, which is part of the *FullProf Suite* package of programs.[28]

Magnetic measurements were performed on a SQUID magnetometer (Quantum Design, MPMS-XL-7T) between 2 and 400 K in different applied fields under both zero-field-cooled (ZFC) and field-cooled on cooling (FCC) conditions. Isothermal magnetization measurements were performed between −70 and 70 kOe at T = 5 K. Frequency dependent ac susceptibility measurements were performed with a Quantum Design MPMS-1T instrument at different frequencies (f) and different applied oscillating magnetic fields (H_{ac}). Specific heat, C_p, at magnetic fields of 0 and 90 kOe was recorded between 2 and 300 K on cooling and heating by a pulse relaxation method using a commercial calorimeter (Quantum Design PPMS). Dielectric properties were measured using a NOVOCONTROL Alpha-A High Performance Frequency Analyzer between 3 and 300 K on cooling and heating in the frequency range of 100 Hz and 2 MHz and at H = 0 and 90 kOe.

3. RESULTS AND DISCUSSION

3.1. Structural Properties of $(Lu_{1-x}Mn_x)MnO_3$.

Compositional dependence of the lattice parameters of $(Lu_{1-x}Mn_x)MnO_3$ ($0 \leq x \leq 0.5$) is shown in Figure 1. The lattice parameters and unit cell volume change monotonically for the samples with $0 \leq x \leq 0.4$, which were single phase, while the saturation-like behavior is observed in $(Lu_{0.5}Mn_{0.5})MnO_3$, which contained about 12 wt % of Mn_2O_3 impurity (the end member of the quasi-binary Lu_2O_3−Mn_2O_3 system). These results suggest that the $(Lu_{1-x}Mn_x)MnO_3$ solid solutions are formed for $0 \leq x \leq 0.4$ under the synthesis conditions used (see also Figure S1). Figures 2 and 3 show the temperature dependence of the orthorhombic lattice parameters (*a*, *b*, and *c*) and the unit cell volume (*V*) for $(Lu_{0.9}Mn_{0.1})MnO_3$ below T = 65 K and $(Lu_{0.6}Mn_{0.4})MnO_3$ below T = 230 K based on powder neutron diffraction data. In both compounds, *b* (interlayer direction) shows a more pronounced temperature dependence than *a* and *c* (intralayer directions). In $(Lu_{0.9}Mn_{0.1})MnO_3$, *b* monotonically decreases toward lower temperature, whereas *a* and *c* remain almost constant. In $(Lu_{0.6}Mn_{0.4})MnO_3$, a pronounced minimum at T_C = 118 K is observed for *b*. Below T_C, decreasing intralayer distances (*a* and *c*) compensate for the increasing interlayer distance (*b*).

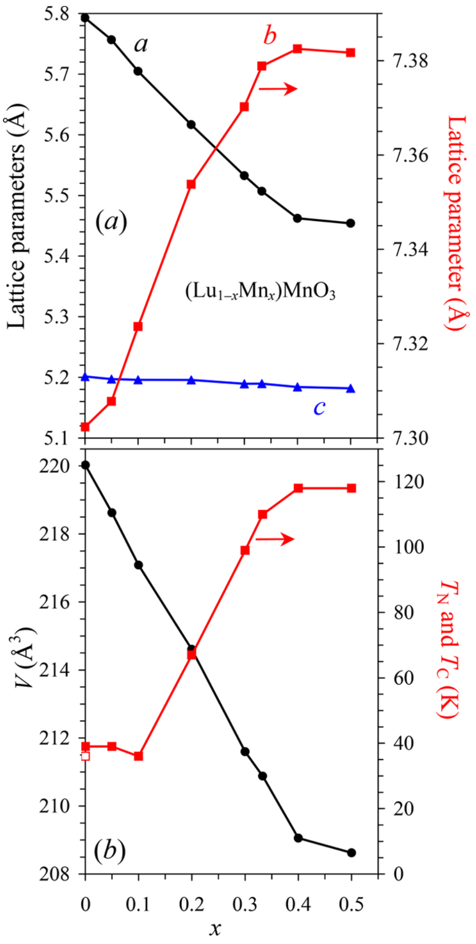

Figure 1. Compositional dependence of (a) the orthorhombic lattice parameters (a, b, and c) and (b) unit cell volume and magnetic transition temperatures in the $(Lu_{1-x}Mn_x)MnO_3$ solid solutions with $0 \leq x \leq 0.5$. T_N is the antiferromagnetic Néel temperature, and T_C is the ferrimagnetic Curie temperature. Note that there are two Néel temperatures, T_{N1} (a filled square) and T_{N2} (an open square) in o-$LuMnO_3$.

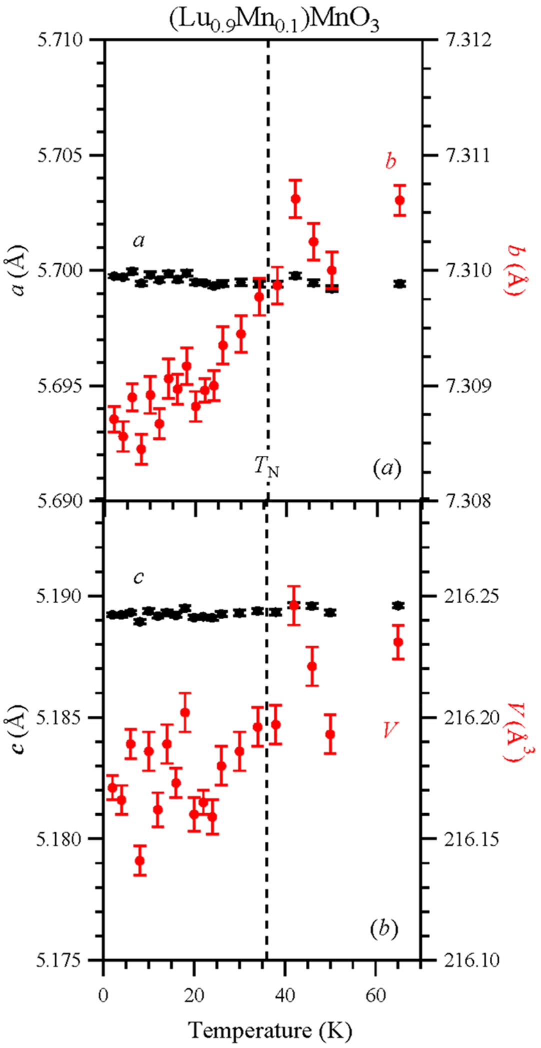

Figure 2. Temperature dependence of the orthorhombic lattice parameters (a, b, and c) and the unit cell volume (V) in $(Lu_{0.9}Mn_{0.1})MnO_3$ refined from neutron diffraction data. The vertical dashed line indicates $T_N = 36$ K.

Both $(Lu_{0.9}Mn_{0.1})MnO_3$ and $(Lu_{0.6}Mn_{0.4})MnO_3$ samples exhibited significant anisotropic broadening of some reflections. Strain broadening was modeled for (100) anisotropic broadening in an orthorhombic lattice using quartic form in reciprocal space.[29,30] Orthorhombic symmetry allows six independent anisotropic strain parameters S_{HKL}.[30] Four of them (e.g., S_{040}, S_{004}, S_{220}, and S_{022}) turned out to be zero within experimental error, whereas the other two parameters, S_{400} and S_{202}, significantly deviated from zero and were refined. The Rietveld refinements without strain corrections had inferior quality as shown in Figure S2a. Obtained structural parameters of o-$LuMnO_3$ (given for comparison), $(Lu_{0.9}Mn_{0.1})MnO_3$, and $(Lu_{0.6}Mn_{0.4})MnO_3$; strain parameters; bond lengths; Mn−O−Mn bond angles; and bond-valence sums (BVS)[31] are summarized in Tables 1 and 2. Experimental, calculated, and difference neutron diffraction patterns measured in the paramagnetic state are shown for $(Lu_{0.9}Mn_{0.1})MnO_3$ at $T = 65$ K in Figure 4a and for $(Lu_{0.6}Mn_{0.4})MnO_3$ at $T = 130$ K in Figure 5a.

With the large contrast between the neutron scattering lengths of Lu and Mn ($b_{Lu} = 7.21$ fm and $b_{Mn} = -3.73$ fm), neutron data are sensitive to the occupation of Lu^{3+} and Mn^{2+} at the A site. The refinements gave the nominal composition (within experimental accuracy) for $(Lu_{0.9}Mn_{0.1})MnO_3$ and a slightly higher Lu^{3+} content (60.9%) for $(Lu_{0.6}Mn_{0.4})MnO_3$. We emphasize that the refinements of the occupation factors of the oxygen sites gave values equal to 1 within experimental errors (for example, $g(O1) = 0.995(9)$ and $g(O2) = 1.009(9)$ in $(Lu_{0.6}Mn_{0.4})MnO_3$). This fact shows that there is no oxygen nonstoichiometry in our samples. Synchrotron X-ray data on $(Lu_{0.667}Mn_{0.333})MnO_3$ detected a splitting of Lu^{3+} and Mn^{2+} (with different oxidation states and masses) at the A site.[26] Neutron data have a lower instrumental resolution and are not so sensitive to such a split-atom model; however, a split-atom model was applied to have consistency with the results from synchrotron X-ray data.[26] For $(Lu_{0.6}Mn_{0.4})MnO_3$, our neutron refinements with no splitting tend to give a negative value for the Debye−Waller factor at the A site ($B = -0.31(5)$ Å^2, $\chi^2 = 2.62$). When allowing two different values for the Debye−Waller factors of Lu^{3+} and Mn^{2+} at the A site, the negative value for B was retained. However, when allowing a splitting similar to the synchrotron X-ray results, we could obtain neutron refinements of a similar quality and a positive value for the Debye−Waller factor at the A site ($B = 0.10$ Å^2, $\chi^2 = 2.64$). In Table 1, we refined the splitting of Lu^{3+} and Mn^{2+} at the A

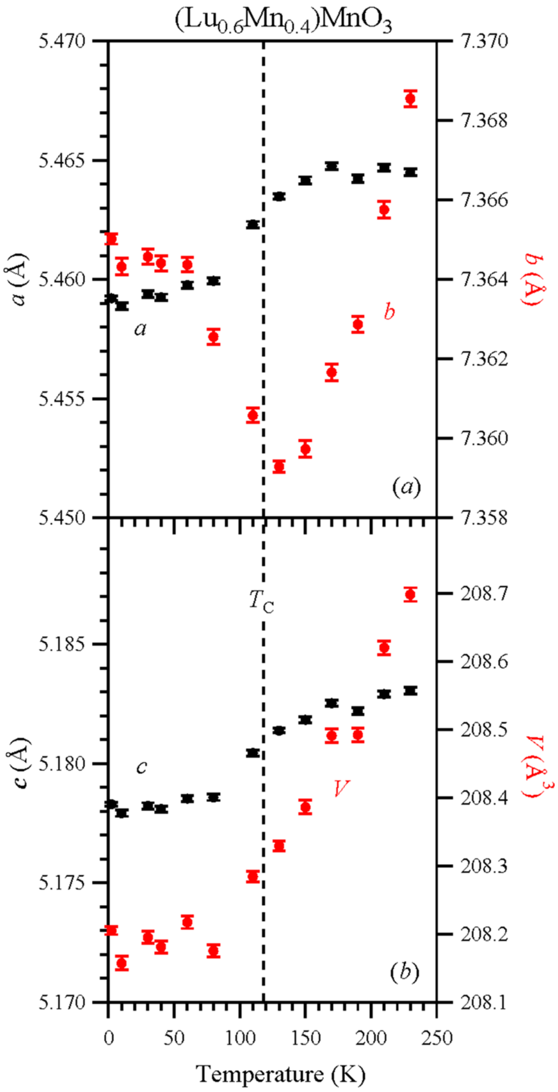

Figure 3. Temperature dependence of the orthorhombic lattice parameters (a, b, and c) and the unit cell volume (V) in $(Lu_{0.6}Mn_{0.4})MnO_3$ refined from neutron diffraction data. The vertical dashed line indicates T_C = 118 K.

site and the occupation factors using the Debye−Waller factor fixed to B = 0.10 Å^2 to prevent correlations between occupation factors and the B parameter. For a refinement without splitting and the fixed B = 0.10 Å^2, the agreement value of the fit increased to χ^2 = 2.68. We emphasize that no split-atom models were used in $(Lu_{0.9}Mn_{0.1})MnO_3$ because of a small concentration of Mn^{2+} at the A site.

The BVS[31] values of the Lu atoms are close to the expected value of +3, while the BVS values of the Mn1 atoms at the A site support the oxidation state of +2. The BVS values of the Mn2 atoms at the B site (+3.20−3.24) of o-$LuMnO_3$ and $(Lu_{0.9}Mn_{0.1})MnO_3$ are noticeably higher than +3. The same features are observed in many manganites with Mn^{3+} and caused by strong Jahn−Teller distortions. The $Mn2O_6$ octahedra have a noticeable elongated Jahn−Teller distortion in o-$LuMnO_3$ (seen as a large octahedral distortion parameter, Δ(Mn2)), and a strong octahedral distortion survives in $(Lu_{0.9}Mn_{0.1})MnO_3$ because of the presence of a large concentration of Mn^{3+} at the B site. On the other hand, the distortion parameter was significantly reduced in $(Lu_{0.6}Mn_{0.4})MnO_3$ because of the presence of a much smaller concentration of Mn^{3+} at the B site. The BVS value of the Mn2 atom in $(Lu_{0.6}Mn_{0.4})MnO_3$ (+3.46) was close to the average oxidation state of +3.4. We note that the Mn−O−Mn bond angles increase in the $(Lu_{1-x}Mn_x)MnO_3$ solid solutions with increasing x.

3.2. Magnetic Structures of $(Lu_{1-x}Mn_x)MnO_3$.

3.2.1. Magnetic Structure of $(Lu_{0.9}Mn_{0.1})MnO_3$. On cooling $(Lu_{0.9}Mn_{0.1})MnO_3$ to T = 2 K, additional magnetic reflections are observed in the neutron diffraction pattern shown in Figure 4b with the strongest magnetic intensity at 2θ = 17.0°. Magnetic reflections correspond to IC magnetic ordering of Mn moments at the B site with a propagation vector of $\mathbf{k} = (k_0, 0, 0)$, where k_0 = 0.438(1) is the magnetic modulation along the a axis. Possible models for the magnetic structures based on group theory analysis[28,32] are summarized in Table 3. For Mn atoms at the B site, the decomposition into four irreducible representations Γ_i is Γ_{Mn} (B site) = $3(\Gamma_1 + \Gamma_2 + \Gamma_3 + \Gamma_4)$.

Each representation is one-dimensional and appears three times. Basis vectors are complex. The observed magnetic structure belongs to Γ_2. The Rietveld refinement confirmed that $(Lu_{0.9}Mn_{0.1})MnO_3$ exhibits a similar IC structure as was reported[13] for o-$LuMnO_3$ between T_{N1} = 39 K and T_{N2} = 36 K (described in ref 13 by using the *Pbnm* setting of space group *Pnma*). The magnetic structure of $(Lu_{0.9}Mn_{0.1})MnO_3$ at 2 K is summarized in Table S1 and shown[33] in Figures 6a, S3a, and S4. The refinement gave no evidence for a contribution from 10% of magnetic Mn^{2+} ions at the A site to the observed magnetic reflections. Therefore, the contribution could be below the detection limit, or Mn^{2+} at the A site could remain magnetically disordered. The magnetic structure is described by a single order parameter with an average amplitude for the 90% Mn^{3+} and 10% Mn^{4+} ions at the B site given by $m_{IC} = \sqrt{2}\,(u, v, w) = \sqrt{2}\,(2.01(2), 0.0(2), 0.75(3))\mu_B$. Within the experimental accuracy ($v = 0.0(2)\mu_B$), the ordered Mn moments lie inside the ac plane. For $Mn2_1$ (0, 0, 1/2), the propagation of spin is given by

$$\mathbf{S}_1(x) = u\cos(k_0 x)\mathbf{e}_x + |w|\cos(k_0 x + \varphi)\mathbf{e}_z$$

Our neutron diffraction experiment can determine the amplitudes u (along x) and w (along z) but not the coupling between them, which may be complex (phase φ). For arbitrary values ($\varphi \neq 0$ and $\varphi \neq \pi$), the magnetic structure is a *cycloid* (illustrated in Figure S4a for $\varphi = \pi/2$), where both direction and size of the ordered Mn moments change. Such a magnetic structure is noncentrosymmetric. In the special cases ($\varphi = 0$ or $\varphi = \pi$), the magnetic structure is *amplitude modulated* (illustrated in Figure S4b for $\varphi = 0$) with the ordered Mn moments varying between $\pm 3.04(3)\mu_B$ $(= \pm\sqrt{2}\,\sqrt{(u^2 + w^2)})$ by forming an angle of about ±20° with the a axis inside the ac plane. Such a magnetic structure is centrosymmetric. Both structures shown in Figure S4 agree equally well with the observed neutron diffraction data, and the phase φ could not be determined. Depending on the value of φ, the magnetic structure of $(Lu_{0.9}Mn_{0.1})MnO_3$ at T = 2 K is centrosymmetric or noncentrosymmetric. We checked for the possibility of a *collinear* amplitude modulated structure with all ordered Mn moments parallel to the a axis ($|w| = 0$). The refinement favors the *noncollinear* structure ($|w| \neq 0$, χ^2 = 2.29) over the *collinear* structure ($|w| = 0$, χ^2 = 2.37). Further, we checked for the possibility of a magnetic structure with ordered Mn moments of a constant size. Compared to the determined magnetic structure (χ^2 = 2.29), the agreement of the refinement

DOI: 10.1021/acs.inorgchem.8b01470
Inorg. Chem. XXXX, XXX, XXX−XXX

Table 1. Structure Parameters of o-$LuMnO_3$ at T = 50 K,[13] $(Lu_{0.9}Mn_{0.1})MnO_3$ at T = 65 K, and $(Lu_{0.6}Mn_{0.4})MnO_3$ at T = 130 K Refined from Powder Neutron Diffraction Data[a–d]

site	WP	g	x	y	z	B (Å^2)
o-$LuMnO_3$, T = 50 K						
Lu	4c	1	0.0857(3)	0.25	0.9815(3)	0.81(4)
Mn2	4b	1	0	0	0.5	1.04(7)
O1	4c	1	0.4580(3)	0.25	0.1217(4)	0.77(4)
O2	8d	1	0.3313(3)	0.0567(2)	0.6987(3)	0.94(3)
$(Lu_{0.9}Mn_{0.1})MnO_3$, T = 65 K						
Lu	4c	0.898(3)	0.0847(2)	0.25	0.9812(2)	0.11(3)
Mn1	4c	0.102(3)	= x(Lu)	0.25	= z(Lu)	= B(Lu)
Mn2	4b	1	0	0	0.5	0.20(3)
O1	4c	1	0.4573(2)	0.25	0.1179(2)	0.44(3)
O2	8d	1	0.3254(2)	0.0563(1)	0.6963(2)	0.46(2)
$(Lu_{0.6}Mn_{0.4})MnO_3$, T = 130 K						
Lu	4c	0.609(1)	0.0818(8)	0.25	0.9701(9)	0.10
Mn1	4c	0.391(1)	0.0867(22)	0.25	0.9507(25)	= B(Lu)
Mn2	4b	1	0	0	0.5	0.25(3)
O1	4c	1	0.4568(2)	0.25	0.1101(2)	0.56(2)
O2	8d	1	0.3120(1)	0.0549(1)	0.6918(1)	0.89(2)

[a] Crystal data: space group $Pnma$ (No 62); Z = 4. WP = Wyckoff position. g is the occupation factor. The Mn2 notation is used in all compounds to mark Mn at the B sites for the uniformity. [b] a = 5.7779(1) Å, b = 7.2998(1) Å, c = 5.1932(1) Å, and V = 219.034(6) Å^3; χ^2 = 5.11, R_{wp} = 6.43%, R_{exp} = 2.84%, and R_{Bragg} = 3.74%; for o-$LuMnO_3$ at T = 50 K. [c] a = 5.6994(1) Å, b = 7.3106(1) Å, c = 5.1896(1) Å, and V = 216.231(7) Å^3; strain parameters [in units of 10^{-4}]: S_{400} = 0.85(2), S_{202} = 1.41(7); χ^2 = 1.68, R_{wp} = 4.59%, R_{exp} = 3.54%, and R_{Bragg} = 1.92%; for $(Lu_{0.9}Mn_{0.1})MnO_3$ at T = 65 K. [d] a = 5.4635(1) Å, b = 7.3593(1) Å, c = 5.1814(1) Å, and V = 208.329(7) Å^3; strain parameters [in units of 10^{-4}]: S_{400} = 0.61(2), S_{202} = 0.54(5); χ^2 = 2.64, R_{wp} = 3.32%, R_{exp} = 2.05%, and R_{Bragg} = 2.92%; for $(Lu_{0.6}Mn_{0.4})MnO_3$ at T = 130. K.

Table 2. Selected Bond Lengths (Å), Bond Angles (deg), Bond Valence Sums, BVS, and Distortion Parameters of MnO_6 (Δ(Mn)) of o-$LuMnO_3$ at T = 50 K,[13] $(Lu_{0.9}Mn_{0.1})MnO_3$ at T = 65 K, and $(Lu_{0.6}Mn_{0.4})MnO_3$ at T = 130 K[a]

	o-$LuMnO_3$ T = 50 K	$(Lu_{0.9}Mn_{0.1})MnO_3$ T = 65 K	$(Lu_{0.6}Mn_{0.4})MnO_3$ T = 130 K
Lu−O1	2.189(3)	2.2035(15)	2.174(5)
Lu−O2 (×2)	2.242(2)	2.2443(11)	2.222(3)
Lu−O1	2.271(2)	2.2391(15)	2.280(5)
Lu−O2 (×2)	2.482(2)	2.4642(12)	2.392(4)
Lu−O2 (×2)	2.5524(17)	2.5543(10)	2.587(2)
BVS(Lu^{3+})	2.88	2.91	3.05
Mn1−O1		2.2035(15)	2.182(12)
Mn1−O2 (×2)		2.2443(11)	2.206(9)
Mn1−O1		2.2391(15)	2.383(15)
Mn1−O2 (×2)		2.4642(12)	2.318(11)
Mn1−O2 (×2)		2.5543(10)	2.626(8)
BVS(Mn^{2+})		1.79	1.89
Mn2−O1 (×2)	1.9465(7)	1.9427(4)	1.9406(3)
Mn2−O2 (×2)	1.8894(16)	1.9090(8)	1.9413(7)
Mn2−O2 (×2)	2.2137(17)	2.1555(8)	2.0140(7)
BVS($Mn2^{3+}$)	3.20	3.24	3.46
Δ(Mn2)	49.1×10^{-4}	29.7×10^{-4}	3.1×10^{-4}
Mn2−O1−Mn2 (×2)	139.29(3)	140.37(2)	142.90(1)
Mn2−O2−Mn2 (×4)	142.30(7)	142.89(3)	144.30(3)

[a] BVS = $\sum_{i=1}^{N} \nu_i$, $\nu_i = \exp[(R_0 - l_i)/B]$, N is the coordination number, B = 0.37, $R_0(Lu^{3+})$ = 1.971, $R_0(Mn^{2+})$ = 1.79, and $R_0(Mn^{3+})$ = 1.76.[31] $\Delta = (1/N)\sum_{i=1}^{N}[(l_i - l_{av})/l_{av}]^2$, where $l_{av} = (1/N)\sum_{i=1}^{N} l_i$ is the average Mn−O distance and N is the coordination number.

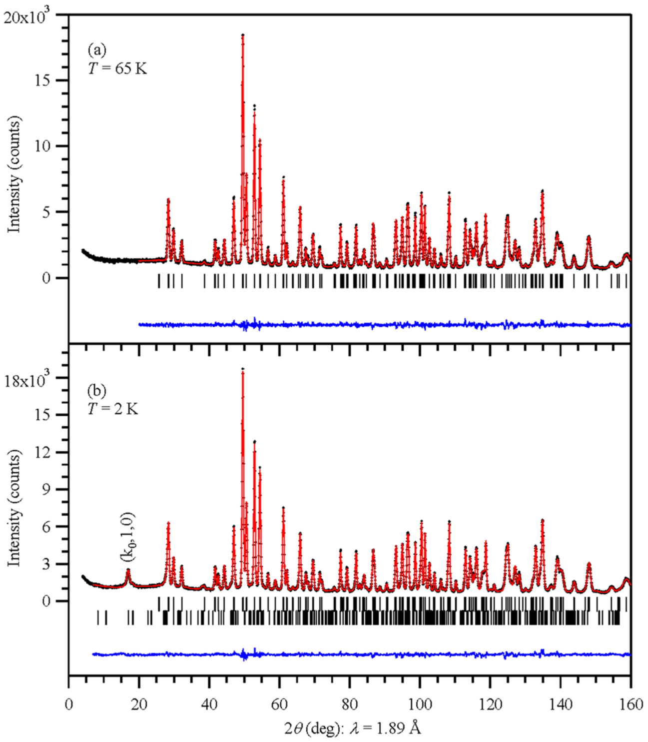

Figure 4. Experimental (black crosses), calculated (red line), and difference (blue line) neutron diffraction patterns of $(Lu_{0.9}Mn_{0.1})MnO_3$ (a) in the paramagnetic state at T = 65 K and (b) in the magnetically ordered state at T = 2 K. The tick marks indicate positions of Bragg reflection positions: the first row is for the nuclear peaks, and the second row is for the magnetic peaks.

deteriorated to χ^2 = 4.08 for a noncentrosymmetric cycloid magnetic structure with ordered Mn moments of a constant size lying inside the ac plane ($u = |w|$, $\varphi = \pi/2$), and even to χ^2 = 6.75 for a noncentrosymmetric helix magnetic structure with ordered Mn moments of a constant size lying inside the bc plane. The temperature dependence of the magnetic structures

DOI: 10.1021/acs.inorgchem.8b01470
Inorg. Chem. XXXX, XXX, XXX−XXX

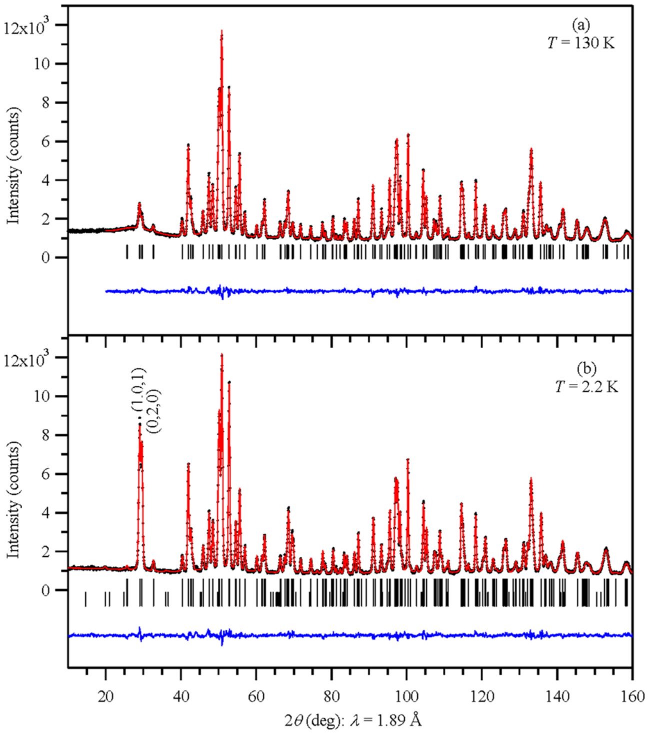

Figure 5. Experimental (black crosses), calculated (red line), and difference (blue line) neutron diffraction patterns of $(Lu_{0.6}Mn_{0.4})MnO_3$ (a) in the paramagnetic state at $T = 130$ K and (b) in the magnetically ordered state at $T = 2.2$ K. The tick marks indicate positions of Bragg reflection positions: the first row is for the nuclear peaks, and the second row is for the magnetic peaks. The strongest magnetic peaks are (1,0,1) at $2\theta = 29.1°$ and (0,2,0) at $2\theta = 29.7°$.

Table 3. Magnetic Arrangement Allowed at the B Site (*4b*) for Each of the Irreducible Representations (IR) Based on Group Theory Analysis (Program *BasIrep*)[28] for Space Group *Pnma* (No. 62 in International Tables for Crystallography)[32] and Incommensurate Magnetic Propagation Vector k = (k_0, 0, 0)[a]

IR	$Mn2_1$ (0, 0, 1/2)	$Mn2_2$ (1/2, 0, 0)	$Mn2_3$ (0, 1/2, 1/2)	$Mn2_4$ (1/2, 1/2, 0)
Γ_1	(u, v, w)	$a^* (-u, -v, w)$	$(u, -v, w)$	$a^* (-u, v, w)$
Γ_2	(u, v, w)	$a^* (u, v, -w)$	$(-u, v, -w)$	$a^* (-u, v, w)$
Γ_3	(u, v, w)	$a^* (-u, -v, w)$	$(-u, v, -w)$	$a^* (u, -v, -w)$
Γ_4	(u, v, w)	$a^* (u, v, -w)$	$(u, -v, w)$	$a^* (u, -v, -w)$

[a] $a^* = \exp(-i\pi k_0)$

of o-$LuMnO_3$ and $(Lu_{0.9}Mn_{0.1})MnO_3$ are compared in Figure 7. In o-$LuMnO_3$, the k_0 component of the propagation vector shows a strong temperature dependence starting with $k_0 = 0.47$ at $T_{N1} = 39$ K and increasing toward the commensurate value $k_0 = 0.50$ at $T_{N2} = 36$ K (Figure 7b). At the same time, the correlation length of the magnetic structure of o-$LuMnO_3$ increases from ~20 nm (at $T_{N1} = 39$ K) toward ~180 nm at 2 K (Figure 7a). In contrast, for $(Lu_{0.9}Mn_{0.1})MnO_3$, the k_0 component increases from $k_0 = 0.425(4)$ at $T = 34$ K (close to $T_N = 36$ K) toward a temperature independent value of $k_0 = 0.438(1)$ below a lock-in transition around $T_2 \approx 24$ K (Figures 7b, S5). Compared to o-$LuMnO_3$, broad magnetic Bragg peaks in $(Lu_{0.9}Mn_{0.1})MnO_3$ give rise to a much shorter correlation length of the magnetic structure starting from ~7 nm at 34 K and reaching only ~21 nm at low temperatures (Figure 7a). The temperature dependence of correlation length and magnetic propagation vector of $(Lu_{0.9}Mn_{0.1})MnO_3$ are shown with expanded scale in Figure S5. The ordered Mn moments $\langle M \rangle$ of the incommensurate structures reach similar values at saturation ($T = 2$ K) in $(Lu_{0.9}Mn_{0.1})MnO_3$ and at T_{N2} in o-$LuMnO_3$ (Figure 7c). Between 26 and 34 K, the intensities $\langle M \rangle$ for $(Lu_{0.9}Mn_{0.1})MnO_3$ in Figure 7c seem to be slightly too large, because they may contain a contribution from diffuse critical scattering around T_N (short-range correlations with the same local structure). Close to T_N, our diffraction data collected with thermal neutrons ($\lambda = 1.89$ Å) have limited accuracy. For o-$LuMnO_3$, the data between T_{N1} and T_{N2} shown in Figure 7c were measured with increased resolution using cold neutrons ($\lambda = 4.5$ Å).

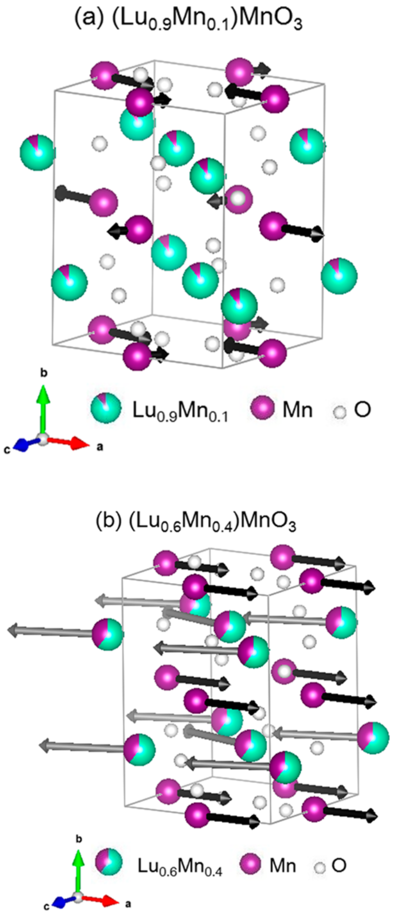

Figure 6. Illustration of the magnetic structures determined for (a) $(Lu_{0.9}Mn_{0.1})MnO_3$ at $T = 2$ K and (b) $(Lu_{0.6}Mn_{0.4})MnO_3$ at $T = 2.2$ K. In $(Lu_{0.9}Mn_{0.1})MnO_3$, an incommensurate spin structure is observed for Mn^{3+} and Mn^{4+} at the B site, and Mn^{2+} at the A site is disordered. $(Lu_{0.6}Mn_{0.4})MnO_3$ adopts a commensurate ferrimagnetic-type spin structure with all Mn ions ordered. The lengths of the arrows are proportional to the magnetic moments per Mn. Additional 2D projections of the magnetic structures on the *ac* plane are shown in Figures S3 and S4. This drawing was made using the program VESTA.[33]

The IC structure of $(Lu_{0.9}Mn_{0.1})MnO_3$ is quite common in undoped perovskites $RMnO_3$ with heavy rare-earth elements (R = Dy−Lu) and Y below the first magnetic ordering temperature.[8,11,34] The *noncollinear* structure ($|w| \neq 0$) was observed in $LuMnO_3$,[13] whereas *collinear* structures ($|w| = 0$) were reported for $YMnO_3$,[4] $HoMnO_3$,[2,3] $ErMnO_3$,[35] and

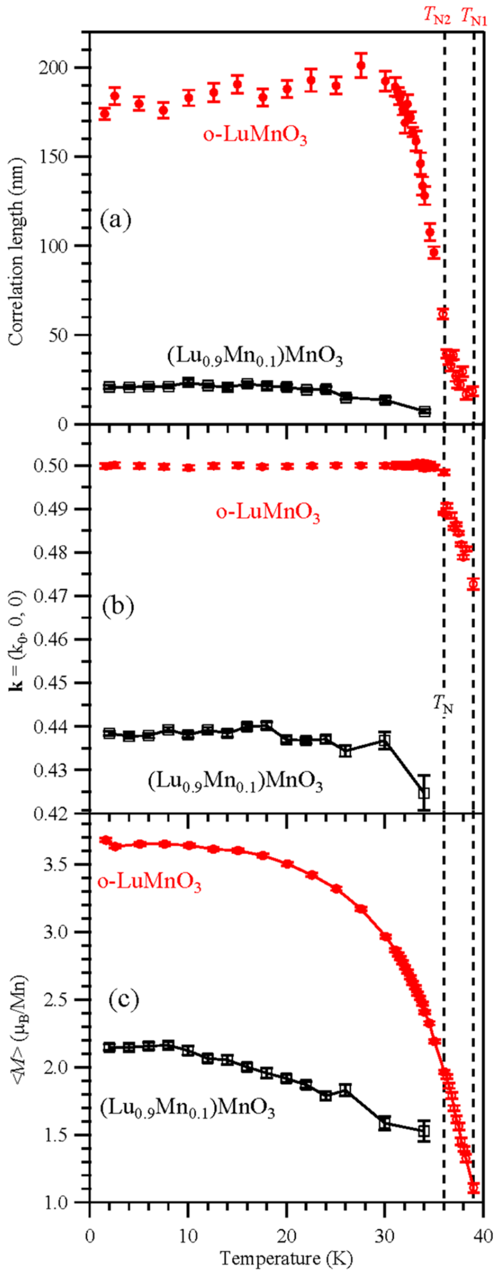

Figure 7. Temperature dependence of the magnetic structures of o-LuMnO$_3$ (from ref 13) with T_{N1} = 39 K and T_{N2} = 36 K and (Lu$_{0.9}$Mn$_{0.1}$)MnO$_3$ with T_N = 36 K. (a) Correlation length, (b) the magnetic propagation vector $\mathbf{k} = (k_0, 0, 0)$, and (c) the magnitude $\langle M \rangle$ of the ordered Mn moment at the B site. Incommensurate structures have an amplitude $|m_{IC}| = \sqrt{2}\,\langle M \rangle$ (notation used in ref 13). Vertical dashed lines indicate T_{N1}, T_{N2}, and T_N. For (Lu$_{0.9}$Mn$_{0.1}$)MnO$_3$, the refinements between 26 and 34 K were performed with a fixed value of $|w|/|u|$ = 0.39 (which corresponds to the average value of the data measured below 20 K). The temperature dependence of correlation length and magnetic propagation vector of (Lu$_{0.9}$Mn$_{0.1}$)MnO$_3$ is shown with expanded scale in Figure S5.

TmMnO$_3$.[10] The stability of the collinear sinusoidal magnetic structure in RMnO$_3$ perovskites was confirmed by theoretical calculations using a replica-exchange Monte Carlo technique.[12] As was shown for HoMnO$_3$,[2,3] besides the exchange parameters associated with the Mn−O−Mn interactions (shorter super exchange paths), also those associated with longer Mn−O−O−Mn exchange paths along the *a* direction are required to stabilize the IC structure. The IC structure is paraelectric (e.g., HoMnO$_3$,[2,3] TmMnO$_3$,[10] LuMnO$_3$,[13] and YMnO$_3$[34]) and changes to a ferroelectric commensurate E-type AFM structure at lower temperatures.[11] (Lu$_{0.9}$Mn$_{0.1}$)MnO$_3$ (this work) belongs to a group of materials where the IC structure remains stable down to low temperatures. Even at the lowest temperature, the IC order has a correlation length of 1 order of magnitude smaller than in the case of a commensurate E-type AFM order. Below the ordering temperature T_N, the magnetic propagation vector shows a weak temperature dependence and then locks onto a temperature independent fixed value at lower temperatures. It is interesting that an IC structure similar to that of (Lu$_{0.9}$Mn$_{0.1}$)MnO$_3$ was found to remain stable down to low temperatures in some samples of o-YMnO$_3$[4] and o-ErMnO$_3$.[35] The IC structures of (Lu$_{0.9}$Mn$_{0.1}$)MnO$_3$, YMnO$_3$, and ErMnO$_3$ are compared in Table 4. In the case of YMnO$_3$,[4] the sample composition was determined to be YMnO$_{3.04(1)}$. In other words, that sample contained about 8% Mn^{4+}. Our (Lu$_{0.9}$Mn$_{0.1}$)MnO$_3$ sample has 10% of Mn^{4+} at the B site. We can assume that the presence of Mn^{4+}, serving as disordered elements, strongly suppresses the temperature evolution of the propagation vector, prevents it from reaching the 0.5 value, and prevents the appearance of the E-type magnetic structure. Therefore, Mn^{4+} at the B site has a crucial role in determining the magnetic behavior of (Lu$_{0.9}$Mn$_{0.1}$)MnO$_3$, and Mn^{2+} at the A site plays a role of any divalent dopant, magnetic or nonmagnetic.

Table 4. Comparison of Incommensurate Magnetic Structures Found to be Stable Down to Low Temperature in (Lu$_{0.9}$Mn$_{0.1}$)MnO$_3$ (this work), YMnO$_3$, and ErMnO$_3$

compound (reference)	(Lu$_{0.9}$Mn$_{0.1}$)MnO$_3$ (this work)	YMnO$_3$ (ref 4)	ErMnO$_3$ (ref 35)
T_N (K)[a]	36	42	42
k_0 (near T_N)	0.425(4)	0.420(4)	≈ 0.415
T_2 (K)[a]	≈ 24	≈ 28	≈ 28
k_0 (below T_2)	0.438(1)	0.435(2)	0.433
u (μ_B)	2.01(2)	2.75(4)	not available
w (μ_B)	0.75(3)	0	not available
kind of magnetic structure:			
-incommensurate, *amplitude modulated or cycloid*			
ordered Mn moments at the B site:			
-propagation vector: $\mathbf{k} = (k_0, 0, 0)$			
-irreducible representation: Γ_2			
-amplitude of ordered Mn moments at low temperature: $m_{IC} = \sqrt{2}\,(u, 0, w)$			

[a] T_N: Neel temperature. T_2: Lock-in temperature.

3.2.2. Magnetic Structure of (Lu$_{0.6}$Mn$_{0.4}$)MnO$_3$. The neutron diffraction pattern measured in the magnetically ordered state of (Lu$_{0.6}$Mn$_{0.4}$)MnO$_3$ at T = 2.2 K is shown in Figure 5b. All magnetic reflections can be indexed with a commensurate propagation vector of $\mathbf{k}$ = (0, 0, 0). The strongest intensities are observed for the magnetic peaks (1, 0, 1) at 2θ = 29.1° and (0, 2, 0) at 2θ = 29.7°. Possible models for the magnetic structures based on group theory analysis[28,36] are summarized in Table 5. For Mn atoms at the B site, four of the eight irreducible representations Γ_i allow magnetic order:

$$\Gamma_{Mn}(\text{B site}) = 3(\Gamma_1 + \Gamma_3 + \Gamma_5 + \Gamma_7)$$

For Mn atoms at the A site, the decomposition is

$$\Gamma_{Mn}(\text{A site}) = \Gamma_1 + \Gamma_4 + \Gamma_5 + \Gamma_8 + 2(\Gamma_2 + \Gamma_3 + \Gamma_6 + \Gamma_7)$$

DOI: 10.1021/acs.inorgchem.8b01470
Inorg. Chem. XXXX, XXX, XXX−XXX

Table 5. Magnetic Arrangement Allowed at the B Site and A Site for Each of the Irreducible Representations (IR) Based on Group Theory Analysis (Program *BasIrep*)[28] for Space Group *Pnma* and Commensurate Magnetic Propagation Vector k = (0, 0, 0)

IR	Mn B site (4*b*)	Mn A site (4*c*)	magnetic space group[36]
Γ_1	(G_x, C_y, A_z)	$(-, c_y, -)$	*Pnma* (No. 62.1.502)
Γ_2		$(g_x, -, a_z)$	*Pn′m′a′* (No. 62.9.510)
Γ_3	(C_x, G_y, F_z)	$(c_x, -, f_z)$	*Pn′m′a* (No. 62.6.507)
Γ_4		$(-, g_y, -)$	*Pnma′* (No. 62.5.506)
Γ_5	(A_x, F_y, G_z)	$(-, f_y, -)$	*Pn′ma′* (No. 62.8.509)
Γ_6		$(a_x, -, g_z)$	*Pnm′a* (No. 62.4.505)
Γ_7	(F_x, A_y, C_z)	$(f_x, -, c_z)$	*Pnm′a′* (No. 62.7.508)
Γ_8		$(-, a_y, -)$	*Pn′ma* (No. 62.3.504)

$F = m_1 + m_2 + m_3 + m_4$ $C = m_1 - m_2 + m_3 - m_4$

$G = m_1 - m_2 - m_3 + m_4$ $A = m_1 + m_2 - m_3 - m_4$

B site: $Mn2_1$ (0, 0, 1/2), $Mn2_2$ (1/2, 0, 0), $Mn2_3$ (0, 1/2, 1/2), $Mn2_4$ (1/2, 1/2, 0)

A site: $Mn1_1$ $(x, 1/4, z)$, $Mn1_2$ $(-x + 1/2, 3/4, z + 1/2)$, $Mn1_3$ $(-x, 3/4, -z)$, $Mn1_4$ $(x + 1/2, 1/4, -z + 1/2)$

The observed magnetic structure of $(Lu_{0.6}Mn_{0.4})MnO_3$ at T = 2.2 K belongs to the irreducible representation Γ_7. The structure is summarized in Table S2 and shown in Figures 6b and S3b. Using the composition determined at T = 130 K (Table 1), the B site is occupied by 60.9% Mn^{3+} and 39.1% Mn^{4+}. The refinement gives an average ordered moment of $(F_x = 3.23(2), A_y = 0.0(2), C_z = 0.0(1))\mu_B$ per Mn atom. The A site is occupied by 39.1% Mn^{2+} and 60.9% nonmagnetic Lu^{3+}. Here, the Mn^{2+} ions order with $(f_x = -4.87(5), 0, c_z = 1.42(8))\mu_B$ per Mn atom. In $(Lu_{0.6}Mn_{0.4})MnO_3$, all ordered Mn moments lie inside the *ac* plane and are dominated by FM components along the *a* direction with the AFM coupling between the B and A sites. Mn^{3+} and Mn^{4+} cations at the B site show *collinear* FM ordering with an average moment of $3.23(2)\mu_B$ along the *a* direction. Mn^{2+} cations at the A site show a *noncollinear* arrangement consisting of an FM component along *a* and an AFM component along *c*. The ordered Mn^{2+} moments of $5.08(17)\mu_B$ form an angle of about ±16° with the *a* direction (Figure S3b). The ferrimagnetic-type structure of $(Lu_{0.6}Mn_{0.4})MnO_3$ contains a net macroscopic FM component along the *a* direction of $1.32(4)\mu_B$ per formula unit. We checked for the possibility of a *collinear* ferrimagnetic structure ($c_z = 0$) with all ordered Mn moments parallel to the *a* direction. The refinement favors a *noncollinear* structure ($\chi^2 = 2.42$) over a *collinear* structure ($\chi^2 = 2.54$). The temperature dependence of the components of the ordered moments at the B and A sites are shown in Figure 8b. The correlation length of the commensurate magnetic structure of $(Lu_{0.6}Mn_{0.4})MnO_3$ (Figure 8a) is much larger than that of the IC structure of $(Lu_{0.9}Mn_{0.1})MnO_3$ (Figure 7a) and comparable to that of o-$LuMnO_3$ (Figure 7a). $NdMn_{0.8}Fe_{0.2}O_3$ (representation Γ_5)[37] is an example of a mixed-cation perovskite with magnetic ordering on the A and B sites similar to $(Lu_{0.6}Mn_{0.4})MnO_3$ (representation Γ_7).

FM arrangements of spins at the B site are realized in $R_{1-x}A_xMnO_3$ manganites with R = La, Pr, Nd, and Sm and A = Ca and Sr in the compositional ranges of about $0.2 \leq x \leq 0.4$.[14−18] The generally accepted mechanism of ferromagnetism is the double-exchange interaction between Mn^{3+} and Mn^{4+} that also leads to metallic conductivities and a noticeable rise of magnetic transition temperatures. We also observed a noticeable rise of magnetic transition temperatures in $(Lu_{1-x}Mn_x)MnO_3$ $(0.2 \leq x \leq 0.4)$ with increasing x (see below and Figure 1), that is, with the increase of the concentration of Mn^{4+}, and the presence of FM interactions between Mn^{3+} and Mn^{4+} at the B site. However, the samples show insulating properties (see dielectric data below). Therefore, a different mechanism could be responsible for FM interactions between Mn^{3+} and Mn^{4+}. We note that narrow compositional ranges with FM insulating properties were also observed in $R_{1-x}A_xMnO_3$ manganites with R = La, Pr, and Nd and A = Ca and Sr.[14−18]

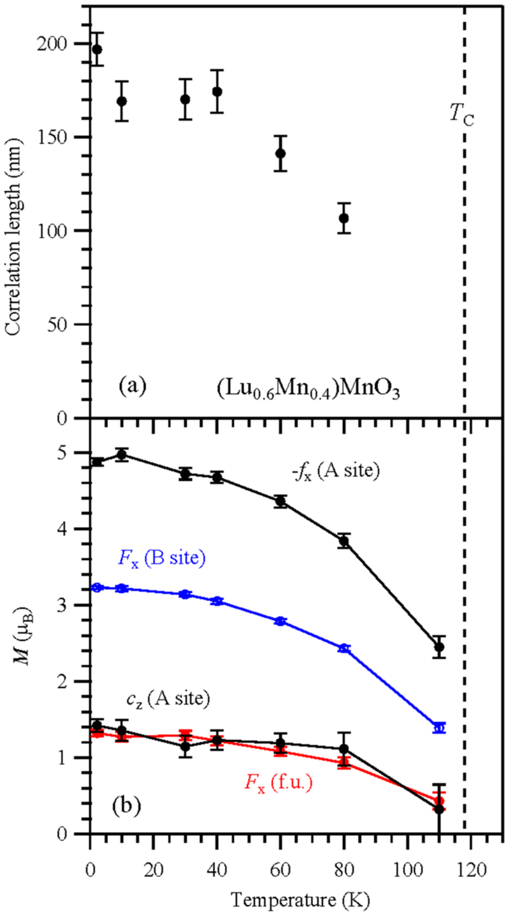

Figure 8. Temperature dependence of the ferrimagnetic structure of $(Lu_{0.6}Mn_{0.4})MnO_3$. (a) Correlation length and (b) ordered Mn moments at A and B sites (per Mn) and net ferromagnetic moment per formula unit of $(Lu_{0.6}Mn_{0.4})MnO_3$ (F_x (f.u.)). The vertical dashed line indicates T_C = 118 K. The determination of the correlation length at 110 K is inaccurate. The refinement at 110 K was performed with the peak shape parameter, *Y*, fixed at the value obtained from the refinement at 80 K.

When R cations are small (e.g., R = Y and Lu), spin-glass magnetic behavior is observed in $Y_{0.7}Ca_{0.3}MnO_3$ and $(Lu_{1-x}Ca_x)MnO_3$ $(0.1 \leq x \leq 0.6)$.[21,38] However, we emphasize that no neutron diffraction experiments were performed in refs 21 and 38 to support the absence of long-range magnetic order. In ref 20, AFM long-range order was found in $(Lu_{0.5}Ca_{0.5})MnO_3$ by neutron powder diffraction. Our neutron diffraction experiments confirmed the presence of long-range magnetic order in $(Lu_{1-x}Mn_x)MnO_3$ $(0.0 \leq x \leq 0.4)$.

3.3. Magnetic and Dielectric Properties of $(Lu_{1-x}Mn_x)MnO_3$. Figures 9−11 and S6 show dc χ vs T magnetic susceptibilities of $(Lu_{1-x}Mn_x)MnO_3$. Isothermal magnetization

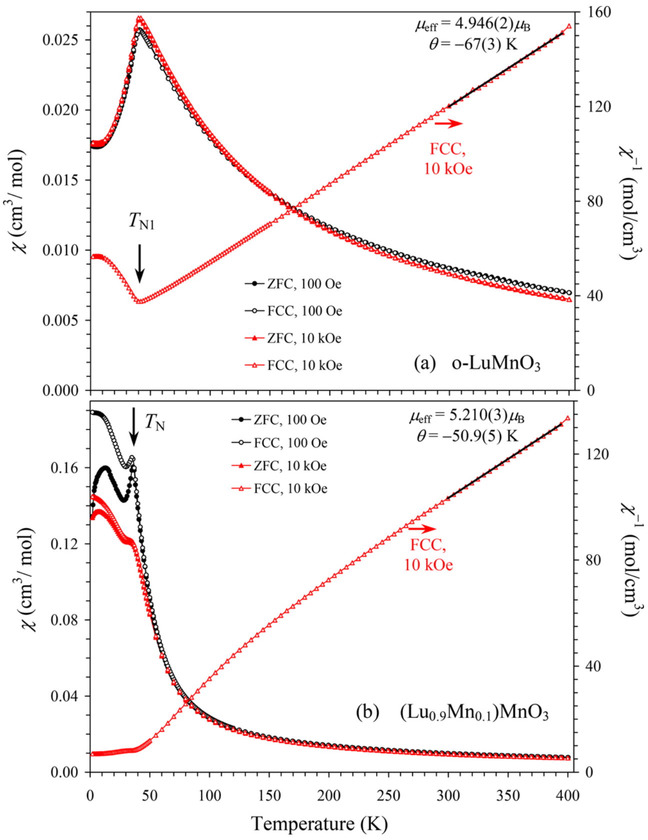

Figure 9. ZFC (filled symbols) and FCC (empty symbols) dc magnetic susceptibility ($\chi = M/H$) curves of (a) o-LuMnO$_3$ and (b) (Lu$_{0.9}$Mn$_{0.1}$)MnO$_3$. Left-hand axes give the χ vs T curves at 100 Oe (black) and 10 kOe (red); right-hand axes give the FCC χ^{-1} vs T curves at 10 kOe with the Curie−Weiss fits.

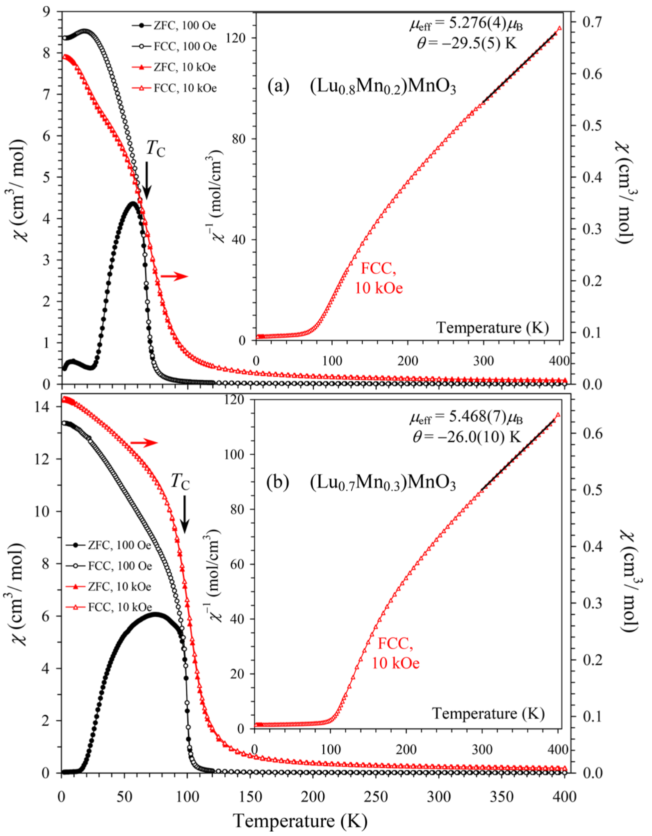

Figure 10. ZFC (filled symbols) and FCC (empty symbols) dc magnetic susceptibility ($\chi = M/H$) curves of (a) (Lu$_{0.8}$Mn$_{0.2}$)MnO$_3$ and (b) (Lu$_{0.7}$Mn$_{0.3}$)MnO$_3$. Left-hand axes give the χ vs T curves at 100 Oe (black); right-hand axes give the χ vs T curves at 10 kOe (red). The insets show the FCC χ^{-1} vs T curves at 10 kOe with the Curie−Weiss fits.

curves (M vs H) are given in Figure 12. The χ vs T curves of o-LuMnO$_3$ were typical for purely AFM materials without any difference between the ZFC and FCC curves even at low magnetic fields. The M vs H curves of o-LuMnO$_3$ were linear without any hysteresis that is also typical for purely AFM materials. A small difference between the ZFC and FCC curves appeared in (Lu$_{0.9}$Mn$_{0.1}$)MnO$_3$, and small hysteresis opened on the M vs H curves indicating the appearance of a small uncompensated moment. However, the hysteresis on the M vs H curves of (Lu$_{0.95}$Mn$_{0.05}$)MnO$_3$ and (Lu$_{0.9}$Mn$_{0.1}$)MnO$_3$ was very "smeared" and had an S-type shape. This behavior is typical for materials with spin-glass-like magnetic properties. Moreover, the propagation vector $\mathbf{k} = (k_0, 0, 0)$ does not support weak FM properties. The appearance of weak FM properties could originate from the induced magnetic moments on Mn at the A site. For $x = 0.05$ and $x = 0.10$, the concentration of Mn^{2+} is still too small to make a long-range magnetic order (at least, detectable by neutron powder diffraction). But an internal field from the B-site ordering and an external magnetic field could align Mn^{2+} and produce the observed weak spin-glass-like FM moment in the magnetization. A large difference between the ZFC and FCC curves appeared in (Lu$_{1-x}$Mn$_x$)MnO$_3$ with $0.2 \leq x \leq 0.4$ at small magnetic fields that is typical for ferrimagnetic materials (and also canted AFM materials). The M vs H curves of (Lu$_{1-x}$Mn$_x$)MnO$_3$ with $x = 1/3$ and 0.4 (with the concentration of Mn^{2+} at the A site above the percolation limit of 0.31 for a cubic net) showed the saturation behavior that is more typical for ferrimagnetic materials. However, we emphasize that the samples with $x = 0.2$ and 0.3 showed a small increase of M with H at high magnetic fields (Figure S7). Magnetic properties of (Lu$_{1-x}$Mn$_x$)MnO$_3$ with $0.2 \leq x \leq 0.4$ are basically consistent with the ferrimagnetic-type structure found by neutron diffraction in (Lu$_{0.6}$Mn$_{0.4}$)MnO$_3$.

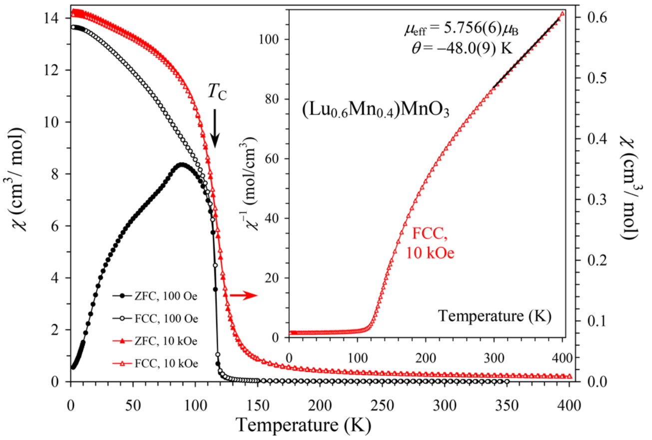

Figure 11. ZFC (filled symbols) and FCC (empty symbols) dc magnetic susceptibility ($\chi = M/H$) curves of (Lu$_{0.6}$Mn$_{0.4}$)MnO$_3$. Left-hand axis gives the χ vs T curves at 100 Oe (black); right-hand axis gives the χ vs T curves at 10 kOe (red). The inset shows the FCC χ^{-1} vs T curves at 10 kOe with the Curie−Weiss fits.

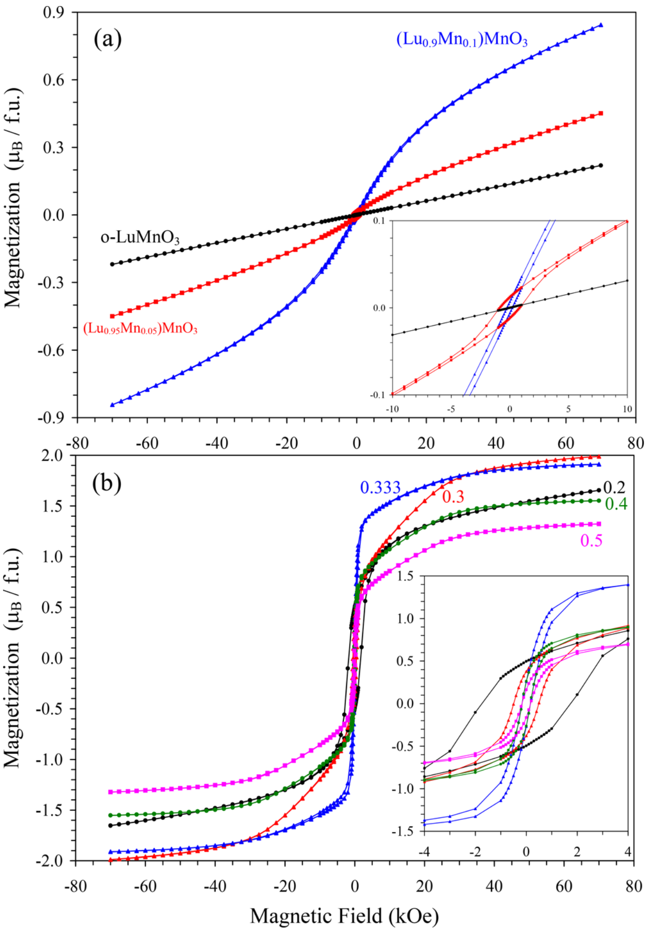

Figure 12. M vs H curves at T = 5 K for (a) $LuMnO_3$, $(Lu_{0.95}Mn_{0.05})MnO_3$, and $(Lu_{0.9}Mn_{0.1})MnO_3$ and (b) $(Lu_{1-x}Mn_x)MnO_3$ solid solutions with x = 0.2, 0.3, 0.333, 0.4, and 0.5. Insets show details near the origin. f.u.: formula unit.

Table 6. Temperatures of Magnetic Anomalies and Parameters of the Curie-Weiss Fits of $(Lu_{1-x}Mn_x)MnO_3$ Solid Solutions[a]

x	T_N or T_C (K)	μ_{eff} (μ_B/f.u.)	μ_{calc} (μ_B/f.u.)	θ (K)	M_S[b] (μ_B/f.u.)
0	36, 39	4.946(2)	4.899	−67(3)	0.22
0.05	39	4.907(5)	5.030	−46.5(7)	0.45
0.1	36	5.210(3)	5.158	−50.9(5)	0.84
0.2	67	5.279(4)	5.404	−29.5(5)	1.65
0.3	99	5.468(7)	5.639	−26.0(10)	1.99
0.333[c]	110	5.488(7)	5.715	−26.7(9)	1.91
0.4	118	5.756(6)	5.865	−48.0(9)	1.55
0.5	118	5.754(11)	6.083	−43.1(2)	1.32

[a] The Curie−Weiss fits are performed between 300 and 395 K for the FCC data at 10 kOe. [b] M_S is the magnetization value at 5 K and 70 kOe. [c] From ref 26.

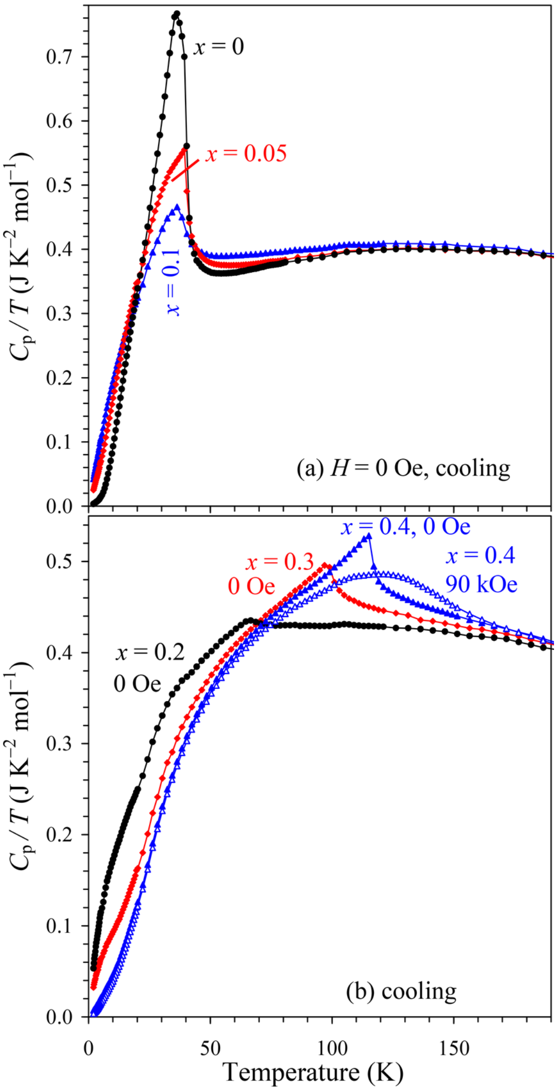

Figure 13. Specific heat data of (a) $LuMnO_3$, $(Lu_{0.95}Mn_{0.05})MnO_3$, and $(Lu_{0.9}Mn_{0.1})MnO_3$ and (b) $(Lu_{0.8}Mn_{0.2})MnO_3$, $(Lu_{0.7}Mn_{0.3})MnO_3$, and $(Lu_{0.6}Mn_{0.4})MnO_3$ plotted as C_p/T vs T. Measurements were performed on cooling at H = 0 Oe. The C_p/T vs T curve on cooling at H = 90 kOe is shown for one sample, $(Lu_{0.6}Mn_{0.4})MnO_3$.

The inverse magnetic susceptibilities follow the Curie−Weiss law. The straight line was observed in o-$LuMnO_3$ almost down to T_{N1} (Figure 9a). However, deviations from the Curie−Weiss law were detected in $(Lu_{1-x}Mn_x)MnO_3$ above T_N especially for $0.2 \leq x \leq 0.4$ (Figures 10 and 11). Such deviations are typical for ferrimagnetic materials,[39] and this behavior is also consistent with the determined magnetic structures.

Between 300 and 395 K, the inverse magnetic susceptibilities (measured at 10 kOe in the FCC mode) are fit by the Curie−Weiss equation (Figure 9 and the insets of Figures 10 and 11)

$$\chi(T) = \mu_{eff}^2 N(3k_B(T - \theta))^{-1}$$

where μ_{eff} is an effective magnetic moment, N is Avogadro's number, k_B is Boltzmann's constant, and θ is the Curie−Weiss temperature. The fitting parameters are summarized in Table 6. The μ_{eff} values are in good agreement with the theoretical values. The negative Curie−Weiss temperatures show that the strongest exchange interactions are AFM in nature.

Figures 13 and S8 and S9 show the C_p/T vs T curves. The specific heat anomalies at T_N do not move, but they are strongly suppressed in $(Lu_{1-x}Mn_x)MnO_3$ with increasing x for $0 \leq x \leq 0.1$ (Figure 13a). On the other hand, the specific heat anomalies move to higher temperatures with increasing x corresponding to the rise of T_C for $0.2 \leq x \leq 0.4$ (Figures 1b and 13b), and the specific heat anomalies are enhanced with increasing x, suggesting that more magnetic entropy is released at T_N with increasing x. The magnetic field had minor effects on the specific heat anomalies for $0 \le x \le 0.1$ (Figure S8), while it significantly smeared the transitions for $0.2 \le x \le 0.4$ (Figures 13b and S9). This behavior is consistent with different magnetic structures in the corresponding compositional ranges.

Figure 14 shows the temperature dependence of a dielectric constant in o-LuMnO$_3$, (Lu$_{0.9}$Mn$_{0.1}$)MnO$_3$, and (Lu$_{0.8}$Mn$_{0.2}$)MnO$_3$. Dielectric data of o-LuMnO$_3$ are in very good agreement with the literature results.[13] Dielectric constant starts increasing when approaching T_{N1} in the IC spin structure, and then it shows a sharp peak at T_{N2}, where the IC phase locks into a commensurate noncollinear E-type structure with a large ferroelectric polarization.[13] In (Lu$_{0.9}$Mn$_{0.1}$)MnO$_3$, we also observed the increase of dielectric constant when approaching T_N (Figure 14a), but because the magnetic structure does not change we found only a small increase and a very broad maximum. According to the reported phase diagrams, the IC-sinusoidal spin structure is not the ground state of any oxygen-stoichiometric RMnO$_3$.[8,11] Therefore, (Lu$_{0.9}$Mn$_{0.1}$)MnO$_3$ provides intrinsic dielectric behavior of the IC-sinusoidal spin structure in the whole temperature range of 3−40 K. Note that similar dielectric behavior was observed in Bi$_{0.1}$Y$_{0.9}$MnO$_3$ and Bi$_{0.2}$Y$_{0.8}$MnO$_3$.[40] In (Lu$_{0.8}$Mn$_{0.2}$)MnO$_3$ with a different magnetic structure, no dielectric anomalies were found at T_C (Figure 14b), and similar dielectric properties were observed in (Lu$_{0.667}$Mn$_{0.333}$)MnO$_3$.[26] The magnetic field of 90 kOe had very minor effects on the values of the dielectric constant in (Lu$_{0.9}$Mn$_{0.1}$)MnO$_3$ and (Lu$_{0.8}$Mn$_{0.2}$)MnO$_3$, suggesting that the magnetodielectric effect is very small. We emphasize that it is quite difficult to correlate dielectric properties with nuclear crystal structures even when clear sharp dielectric anomalies are observed. This is because spin-induced structural polar distortions are so small that they usually cannot be determined from powder diffraction data,[34] and nuclear structures are usually described in centrosymmetric models even below spin-induced ferroelectric transitions. For this reason, we refrain from any discussion on correlations between dielectric properties and atomic displacements.

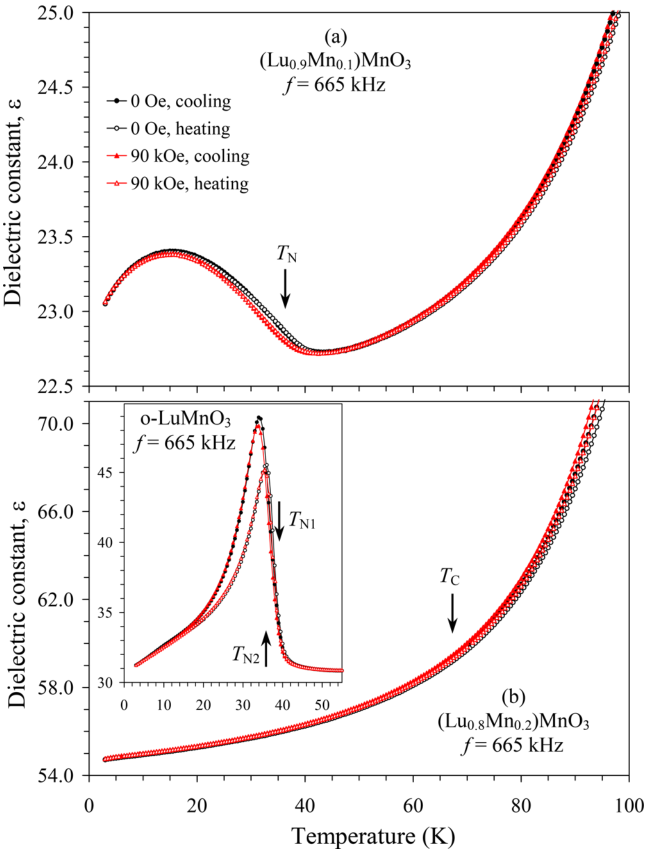

Figure 14. Temperature dependence of the dielectric constant in (a) (Lu$_{0.9}$Mn$_{0.1}$)MnO$_3$ and (b) (Lu$_{0.8}$Mn$_{0.2}$)MnO$_3$. The inset shows dielectric data for o-LuMnO$_3$. Measurements were performed on cooling and heating at H = 0 Oe and 90 kOe (the data at one frequency of 665 kHz are shown).

3.4. Composition−Temperature Phase Diagram of (Lu$_{1-x}$Mn$_x$)MnO$_3$.

Figure 15 shows a composition−temperature phase diagram of the (Lu$_{1-x}$Mn$_x$)MnO$_3$ system with $0 \le x \le 0.4$, which can be constructed based on our magnetic structure determination and physical property measurements. The (Lu$_{1-x}$Mn$_x$)MnO$_3$ phase diagram is noticeably simpler than any phase diagram of R$_{1-x}$A$_x$MnO$_3$ manganites.[14−18,41,42] We emphasize the absence of any FM metallic regions and charge-order transitions and phases. On the other hand, charge-order transitions and regions were found in (R$_{0.5}$Ca$_{0.5}$)MnO$_3$ (R = Tb−Lu) near 200−300 K[19,20,41,42] and many other R$_{1-x}$A$_x$MnO$_3$ phase diagrams. An FM ordering of Mn^{3+} and Mn^{4+} cations at the B site was found in (Lu$_{1-x}$Mn$_x$)MnO$_3$ for $0.2 \le x \le 0.4$ and in other (R$_{1-x}$Mn$_x$)MnO$_3$ systems with R = Ho−Yb for $x \ge 0.2$ (these results will be published elsewhere), while an AFM ordering was suggested in (Lu$_{0.5}$Ca$_{0.5}$)MnO$_3$.[20] Therefore, the presence of Mn^{2+} at the A site makes the difference and promotes a different magnetic structure. The ionic radius of Mn^{2+} ($r_{\rm VIII}$ = 0.96 Å) is smaller than that of Lu^{3+} ($r_{\rm VIII}$ = 0.977 Å).[43] Therefore, the degree of distortion (or the degree of octahedral MnO$_6$ tilting) should increase with increasing x. However, we observed an opposite effect when Mn−O−Mn bond angles became closer to 180° with increasing x (Table 2). This effect is probably caused by the appearance of smaller Mn^{4+} cations ($r_{\rm VI}$ = 0.53 Å) at the B site (cf., $r_{\rm VI}$ = 0.645 Å for Mn^{3+})[43] because the decrease of the average ionic size at the B site overcomes the decrease of the average ionic size at the A site. If only structural distortions (Mn−O−Mn bond angles, which determine the strengths of nearest neighbor and next-nearest neighbor Mn−Mn inter-

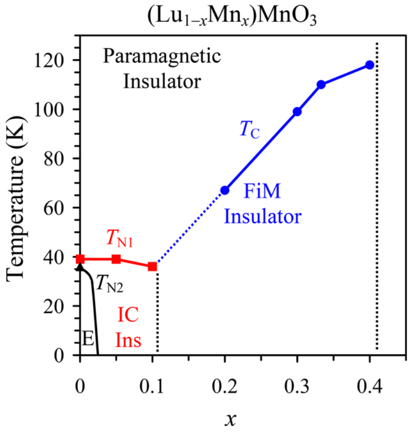

Figure 15. A composition−temperature phase diagram of the (Lu$_{1-x}$Mn$_x$)MnO$_3$ system for $0.0 \le x \le 0.4$. FiM: ferrimagnetic. T_C: FiM Curie temperature. IC: incommensurate. Ins: insulator. E: E-type antiferromagnetic structure. T_N: Néel temperature.

actions) are considered, the $(Lu_{1-x}Mn_x)MnO_3$ system should move to the direction of the $RMnO_3$ systems with larger R cations (R = Er−Yb), where phase diagrams are well-known,[7,8,12] not to an unknown direction with A cations smaller than Lu^{3+}. This basically happened at small doping levels. But the presence of small amounts of Mn^{4+} at the *B* site could act as pinning centers and prevents the development of the propagation vector to the commensurate value as discussed in the end of section 3.2.1. An element of disordering introduced by the presence of Mn^{4+} could also explain a very short correlation length observed in $(Lu_{0.9}Mn_{0.1})MnO_3$. When the doping level increases, Mn^{2+} at the A site becomes involved in the long-range magnetic order. The primary role of magnetic Mn^{2+} cations at the A site for such compositions can be seen from the facts that FM ordering of Mn^{3+} and Mn^{4+} cations at the B site does not depend on the Mn^{4+} concentration, Mn−O−Mn bond angles, and the size and nature of R cations.

4. CONCLUSION

We prepared $(Lu_{1-x}Mn_x)MnO_3$ solid solutions for $0.0 \leq x \leq 0.4$ under high-pressure, high-temperature synthesis conditions at 6 GPa and 1670 K and constructed a composition−temperature phase diagram. The introduction of magnetic Mn^{2+} cations into the A site with the formation of Mn^{4+} at the B site suppresses the appearance of the E-type commensurate magnetic structure, which is the ground state in o-$LuMnO_3$ and freezes an incommensurate spin structure for $x = 0.1$ and finally leads to a ferrimagnetic structure for $x \geq 0.2$. Dielectric properties of $(Lu_{1-x}Mn_x)MnO_3$ are strongly influenced by the underlying magnetic structures. $(Lu_{1-x}Mn_x)MnO_3$ can serve as a model and reference system for future understanding of the behavior of $(R_{1-x}Mn_x)MnO_3$ solid solutions with magnetic rare-earth elements.

■ ASSOCIATED CONTENT

Ⓢ Supporting Information

The Supporting Information is available free of charge on the ACS Publications website at DOI: 10.1021/acs.inorgchem.8b01470.

> Details of neutron powder diffraction patterns, magnetic structures, magnetic and dielectric properties, and refinement results (PDF)

Accession Codes

CCDC 1845241−1845243 contain the supplementary crystallographic data for this paper. These data can be obtained free of charge via www.ccdc.cam.ac.uk/data_request/cif, or by emailing data_request@ccdc.cam.ac.uk, or by contacting The Cambridge Crystallographic Data Centre, 12 Union Road, Cambridge CB21EZ, UK; fax: + 44 1223 336033.

■ AUTHOR INFORMATION

Corresponding Author

*E-mail: Alexei.Belik@nims.go.jp.

ORCID

Kazunari Yamaura: 0000-0003-0390-8244
Alexei A. Belik: 0000-0001-9031-2355

Notes

The authors declare no competing financial interest.

■ ACKNOWLEDGMENTS

This work was supported by JSPS KAKENHI Grant Numbers JP15K14133 and JP16H04501 and JSPS Bilateral Open Partnership Joint Research Projects. This work is partially based on experiments performed on the HRPT diffractometer (Proposal No. 20170092) at the Swiss Spallation Neutron Source SINQ, Paul Scherrer Institute, Switzerland. The authors wish to thank C. Joachim for helpful comments.

■ REFERENCES

(1) Alonso, J. A.; Martıinez-Lope, M. J.; Casais, M. T.; Fernandez-Dıaz, M. T. Evolution of the Jahn-Teller Distortion of MnO_6 Octahedra in $RMnO_3$ Perovskites (R = Pr, Nd, Dy, Tb, Ho, Er, Y): A Neutron Diffraction Study. *Inorg. Chem.* **2000**, *39*, 917−923.

(2) Brinks, H. W.; Rodriguez-Carvajal, R.; Fjellvåg, H.; Kjekshus, A.; Hauback, B. C. Crystal and Magnetic Structure of Orthorhombic $HoMnO_3$. *Phys. Rev. B: Condens. Matter Mater. Phys.* **2001**, *63*, No. 094411, DOI: 10.1103/PhysRevB.63.094411.

(3) Munoz, A.; Casais, M. T.; Alonso, J. A.; Martinez-Lope, M. J.; Martinez, J. L.; Fernandez-Diaz, M. T. Complex Magnetism and Magnetic Structures of the Metastable $HoMnO_3$ Perovskite. *Inorg. Chem.* **2001**, *40*, 1020−1028.

(4) Munoz, A.; Alonso, J. A.; Casais, M. T.; Martinez-Lope, M. J.; Martinez, J. L.; Fernandez-Diaz, M. T. The Magnetic Structure of $YMnO_3$ Perovskite Revisited. *J. Phys.: Condens. Matter* **2002**, *14*, 3285−3294.

(5) Kimura, T.; Goto, T.; Shintani, H.; Ishizaka, K.; Arima, T.; Tokura, Y. Magnetic Control of Ferroelectric Polarization. *Nature (London, U. K.)* **2003**, *426*, 55−58.

(6) Kenzelmann, M.; Harris, A. B.; Jonas, S.; Broholm, C.; Schefer, J.; Kim, S. B.; Zhang, C. L.; Cheong, S.-W.; Vajk, O. P.; Lynn, J. W. Magnetic Inversion Symmetry Breaking and Ferroelectricity in $TbMnO_3$. *Phys. Rev. Lett.* **2005**, *95*, No. 087206, DOI: 10.1103/PhysRevLett.95.087206.

(7) Zhou, J.-S.; Goodenough, J. B. Unusual Evolution of the Magnetic Interactions Versus Structural Distortions in $RMnO_3$ Perovskites. *Phys. Rev. Lett.* **2006**, *96*, 247202.

(8) Tachibana, M.; Shimoyama, T.; Kawaji, H.; Atake, T.; Takayama-Muromachi, E. Jahn-Teller Distortion and Magnetic Transitions in Perovskite $RMnO_3$ (R = Ho, Er, Tm, Yb, and Lu). *Phys. Rev. B: Condens. Matter Mater. Phys.* **2007**, *75*, 144425.

(9) Uusi-Esko, K.; Malm, J.; Imamura, N.; Yamauchi, H.; Karppinen, M. Characterization of $RMnO_3$ (R = Sc, Y, Dy-Lu): High-Pressure Synthesized Metastable Perovskites and Their Hexagonal Precursor Phases. *Mater. Chem. Phys.* **2008**, *112*, 1029−1034.

(10) Pomjakushin, V. Yu.; Kenzelmann, M.; Dönni, A.; Harris, A. B.; Nakajima, T.; Mitsuda, S.; Tachibana, M.; Keller, L.; Mesot, J.; Kitazawa, H.; Takayama-Muromachi, E. Evidence for Large Electric Polarization from Collinear Magnetism in $TmMnO_3$. *New J. Phys.* **2009**, *11*, 043019.

(11) Ishiwata, S.; Kaneko, Y.; Tokunaga, Y.; Taguchi, Y.; Arima, T.; Tokura, Y. Perovskite Manganites Hosting Versatile Multiferroic Phases with Symmetric and Antisymmetric Exchange Strictions. *Phys. Rev. B: Condens. Matter Mater. Phys.* **2010**, *81*, 100411.

(12) Mochizuki, M.; Furukawa, N.; Nagaosa, N. Theory of Spin-Phonon Coupling in Multiferroic Manganese Perovskites $RMnO_3$. *Phys. Rev. B: Condens. Matter Mater. Phys.* **2011**, *84*, 144409.

(13) Mukherjee, S.; Dönni, A.; Nakajima, T.; Mitsuda, S.; Tachibana, M.; Kitazawa, H.; Pomjakushin, V.; Keller, L.; Niedermayer, C.; Scaramucci, A.; Kenzelmann, M. E-type Noncollinear Magnetic Ordering in Multiferroic o-$LuMnO_3$. *Phys. Rev. B: Condens. Matter Mater. Phys.* **2017**, *95*, 104412.

(14) Salamon, M. B.; Jaime, M. The Physics of Magnanites: Structure and Transport. *Rev. Mod. Phys.* **2001**, *73*, 583−628.

(15) Coey, J. M. D.; Viret, M.; von Molnar, S. Mixed-valence Manganites. *Adv. Phys.* **2009**, *58*, 571−697.

(16) Edwards, D. M. Ferromagnetism and Electron-Phonon Coupling in the Manganites. *Adv. Phys.* **2002**, *51*, 1259−1318.

(17) Martin, C.; Maignan, A.; Hervieu, M.; Raveau, B. Magnetic Phase Diagrams of $L_{1-x}A_xMnO_3$ Manganites (L = Pr,Sm; A = Ca,Sr). *Phys. Rev. B: Condens. Matter Mater. Phys.* **1999**, *60*, 12191−12199.

(18) Ivanov, V. Yu.; Mukhin, A. A.; Prokhorov, A. S.; Balbashov, A. M. Phase Transitions in $Sm_{1-x}Sr_xMnO_3$ Single Crystals ($0 \le x \le 0.8$). *Phys. Status Solidi B* **2003**, *236*, 445−449.

(19) Yoshii, K.; Abe, H.; Ikeda, N. Structure, Magnetism and Transport of the Perovskite Manganites $Ln_{0.5}Ca_{0.5}MnO_3$ (Ln = Ho, Er, Tm, Yb, and Lu). *J. Solid State Chem.* **2005**, *178*, 3615−3623.

(20) Martinelli, A.; Ferretti, M.; Cimberle, M. R.; Ritter, C. Neutron Powder Diffraction Analysis of $(Tm_{0.50}Ca_{0.50})MnO_3$ and $(Lu_{0.50}Ca_{0.50})MnO_3$. *J. Solid State Chem.* **2012**, *196*, 314−319.

(21) Imamura, N.; Karppinen, M.; Motohashi, T.; Yamauchi, H. Magnetic and Magnetotransport Properties of the Orthorhombic Perovskites $(Lu,Ca)MnO_3$. *Phys. Rev. B: Condens. Matter Mater. Phys.* **2008**, *77*, No. 024422, DOI: 10.1103/PhysRevB.77.024422.

(22) Zhang, H.; Flacau, R.; Sun, J.; Li, G.; Liao, F.; Lin, J. Synthesis, Structure, and Magnetic Properties of $(Tb_{1-x}Mn_y)MnO_{3-\delta}$. *Inorg. Chem.* **2014**, *53*, 4535−4540.

(23) Zhang, H.; Flacau, R.; Du, X.; Manuel, P.; Cong, J.; Sun, Y.; Sun, J.; Yang, S.; Li, G.; Liao, F.; Lin, J. Multiferroicity Broken by Commensurate Magnetic Ordering in Terbium Orthomanganite. *ChemPhysChem* **2016**, *17*, 1098−1103.

(24) Deng, J.; Farid, M. A.; Zhang, M.; Yang, A.; Zhang, H.; Zhang, H.; Tian, G.; Wu, M.; Liu, L.; Sun, J.; Li, G.; Liao, F.; Lin, J. Enhancement of Ferroelectricity for Orthorhombic $(Tb_{0.861}Mn_{0.121})MnO_{3-\delta}$ by Copper Doping. *Inorg. Chem.* **2017**, *56*, 3475−3482.

(25) Deng, J.; Yang, A.; Farid, M. A.; Zhang, H.; Li, J.; Zhang, H.; Li, G.; Liu, L.; Sun, J.; Lin, J. Synthesis, Structure and Magnetic Properties of $(Eu_{1-x}Mn_x)MnO_{3-\delta}$. *RSC Adv.* **2017**, *7*, 2019−2024.

(26) Zhang, L.; Gerlach, D.; Dönni, A.; Chikyow, T.; Katsuya, Y.; Tanaka, M.; Ueda, S.; Yamaura, K.; Belik, A. A. Mn Self-Doping of Orthorhombic $RMnO_3$ Perovskites: $(R_{0.667}Mn_{0.333})MnO_3$ with R = Er-Lu. *Inorg. Chem.* **2018**, *57*, 2773−2781.

(27) Fischer, P.; Frey, G.; Koch, M.; Könnecke, M.; Pomjakushin, V.; Schefer, J.; Thut, R.; Schlumpf, N.; Bürge, R.; Greuter, U.; Bondt, S.; Berruyer, E. High Resolution Powder Diffractometer HRPT for Thermal Neutrons at SINQ. *Phys. B* **2000**, *276−278*, 146−147.

(28) Rodriguez-Carvajal, J. Recent Advances in Magnetic Structure Determination by Neutron Powder Diffraction. *Phys. B* **1993**, *192*, 55−69.

(29) Rodriguez-Carvajal, R.; Fernandez-Diaz, M. T.; Martinez, J. L. Neutron Diffraction Study on Structural and Magnetic Properties of La_2NiO_4. *J. Phys.: Condens. Matter* **1991**, *3*, 3215−3234.

(30) Stephens, P. W. Phenomenological Model of Anisotropic Peak Broadening in Powder Diffraction. *J. Appl. Crystallogr.* **1999**, *32*, 281−289.

(31) Brese, N. E.; O'Keeffe, M. Bond-Valence Parameters for Solids. *Acta Crystallogr., Sect. B: Struct. Sci.* **1991**, *47*, 192−197.

(32) Hahn, T. *International Tables for Crystallography, Vol. A, Space Group Symmetry*, 5th ed.; Wiley, 2005.

(33) Momma, K.; Izumi, F. VESTA 3 for Three-dimensional Visualization of Crystal, Volumetric and Morphology Data. *J. Appl. Crystallogr.* **2011**, *44*, 1272−1276.

(34) Okuyama, D.; Ishiwata, S.; Takahashi, Y.; Yamauchi, K.; Picozzi, S.; Sugimoto, K.; Sakai, H.; Takata, M.; Shimano, R.; Taguchi, Y.; Arima, T.; Tokura, Y. Magnetically Driven Ferroelectric Atomic Displacements in Orthorhombic $YMnO_3$. *Phys. Rev. B: Condens. Matter Mater. Phys.* **2011**, *84*, No. 054440, DOI: 10.1103/PhysRevB.84.054440.

(35) Ye, F.; Lorenz, B.; Huang, Q.; Wang, Y. Q.; Sun, Y. Y.; Chu, C. W.; Fernandez-Baca, J. A.; Dai, P.; Mook, H. A. Incommensurate Magnetic Structure in the Orthorhombic Perovskite $ErMnO_3$. *Phys. Rev. B: Condens. Matter Mater. Phys.* **2007**, *76*, No. 060402, DOI: 10.1103/PhysRevB.76.060402.

(36) Litvin, D. B. Magnetic Group Tables (International Union of Crystallography, 2013). www.iucr.org/publ/978-0-9553602-2-0.

(37) Mihalik, M.; Mihalik, M.; Hoser, A.; Pajerowski, D. M.; Kriegner, D.; Legut, D.; Lebecki, K. M.; Vavra, M.; Fitta, M.; Meisel, M. W. Magnetic Structure of the Mixed Antiferromagnet $NdMn_{0.8}Fe_{0.2}O_3$. *Phys. Rev. B: Condens. Matter Mater. Phys.* **2017**, *96*, 134430.

(38) Mathieu, R.; Nordblad, P.; Nam, D. N. H.; Phuc, N. X.; Khiem, N. V. Short-range Ferromagnetism and Spin-Glass State in $Y_{0.7}Ca_{0.3}MnO_3$. *Phys. Rev. B: Condens. Matter Mater. Phys.* **2001**, *63*, 174405.

(39) Sanchez-Benitez, J.; Martinez-Lope, M. J.; Alonso, J. A. Preparation at Moderate Pressures, Crystal and Magnetic Structure and Magnetotransport of the Ferrimagnetic $CeCu_3Mn_4O_{12}$ Perovskite. *J. Appl. Phys.* **2010**, *107*, 103904.

(40) Belik, A. A. Structural, Magnetic, and Dielectric Properties of Solid Solutions Between $BiMnO_3$ and $YMnO_3$. *J. Solid State Chem.* **2017**, *246*, 8−15.

(41) Machida, A.; Moritomo, Y.; Ohoyama, K.; Nakamura, A. Neutron Investigation of $Tb_{1-x}Ca_xMnO_3$ ($x \ge 0.5$). *J. Phys. Soc. Jpn.* **2001**, *70*, 3739−3746.

(42) Blasco, J.; Ritter, C.; Garcia, J.; de Teresa, J. M.; Perez-Cacho, J.; Ibarra, M. R. Structural and Magnetic Study of $Tb_{1-x}Ca_xMnO_3$ Perovskites. *Phys. Rev. B: Condens. Matter Mater. Phys.* **2000**, *62*, 5609−5618.

(43) Shannon, R. D. Revised Effective Ionic Radii and Systematic Studies of Interatomic Distances in Halides and Chalcogenides. *Acta Crystallogr., Sect. A: Cryst. Phys., Diffr., Theor. Gen. Crystallogr.* **1976**, *32*, 751−767.